

Models of passive and active dendrite motoneuron pools and their differences in muscle force control

Leonardo Abdala Elias · Vitor Martins Chaud ·
André Fabio Kohn

Received: 9 January 2012 / Revised: 8 April 2012 / Accepted: 16 April 2012 / Published online: 6 May 2012
© Springer Science+Business Media, LLC 2012

Abstract Motoneuron (MN) dendrites may be changed from a passive to an active state by increasing the levels of spinal cord neuromodulators, which activate persistent inward currents (PICs). These exert a powerful influence on MN behavior and modify the motor control both in normal and pathological conditions. Motoneuronal PICs are believed to induce nonlinear phenomena such as the genesis of extra torque and torque hysteresis in response to percutaneous electrical stimulation or tendon vibration in humans. An existing large-scale neuromuscular simulator was expanded to include MN models that have a capability to change their dynamic behaviors depending on the neuromodulation level. The simulation results indicated that the variability (standard deviation) of a maintained force depended on the level of neuromodulatory activity. A force with lower variability was obtained when the motoneuronal network was under a strong influence of PICs, suggesting a functional role in postural and precision tasks. In an additional set of simulations when PICs were active in the dendrites of the MN models, the results successfully reproduced experimental results reported from humans. Extra torque was evoked by the self-sustained discharge of spinal MNs, whereas differences in recruitment and de-recruitment levels of the MNs were the main reason behind torque and

electromyogram (EMG) hysteresis. Finally, simulations were also used to study the influence of inhibitory inputs on a MN pool that was under the effect of PICs. The results showed that inhibition was of great importance in the production of a phasic force, requiring a reduced co-contraction of agonist and antagonist muscles. These results show the richness of functionally relevant behaviors that can arise from a MN pool under the action of PICs.

Keywords Bistability · Nonlinearities in force control · Electromyogram · L-type calcium channel · Persistent inward current · Plateau potential

Abbreviations

AD	Active dendrite
AHP	Afterhyperpolarization
BT	Basal torque
Ca ⁺⁺	Calcium
CV	Coefficient of variation
EMG	Electromyogram
EPSP	Excitatory post-synaptic potential
ET	Extra torque
IPSP	Inhibitory post-synaptic potential
K ⁺	Potassium
LG	Lateral Gastrocnemius
MG	Medial Gastrocnemius
MN	Motoneuron
MT	Maximum torque
MU	Motor unit
Na ⁺	Sodium
PD	Passive dendrite
PIC	Persistent inward current
SOL	Soleus muscle
TA	Tibialis anterior
TS	Triceps Surae

Action Editor: Eberhard Fetz

All authors contributed equally to this work.

L. A. Elias (✉) · V. M. Chaud · A. F. Kohn
Biomedical Engineering Laboratory, Escola Politécnica, PTC,
Universidade de São Paulo, Av. Prof. Luciano Gualberto,
trav. 3, 158, São Paulo, SP, Brazil CEP: 05508-900
e-mail: leoabdala@leb.usp.br

L. A. Elias
e-mail: ee.leoabdala@gmail.com

1 Introduction

The activity of neuromodulatory pathways from the brainstem in a behaving animal (Jacobs and Fornal 1997; Jacobs et al. 2002) has a powerful effect on changes in the intrinsic properties of spinal motoneurons (MNs) and may modify the motor behavior as a whole (Heckman et al. 2005; Heckman et al. 2009). A fundamental intrinsic change is a facilitation of activation of voltage-gated dendritic ionic channels, mainly L-type Ca^{++} channels, which generate a dendritic persistent inward current (PIC) and plateau potentials (Hounsgaard et al. 1988; Lee and Heckman 1998a, b; Schwindt and Crill 1980a, b). This enhances MN excitability and changes the way synaptic inputs are integrated (Binder and Powers 1999; Binder 2002; Heckman and Lee 1999; Hyngstrom et al. 2008; Lee and Heckman 2000).

Several evidences have pointed out the influence of PICs in both normal and pathological motor behaviors. For instance, PICs have been associated with motoneuronal hyperexcitability in chronic spinal cord injury and amyotrophic lateral sclerosis (ElBasiouny et al. 2010; Heckman et al. 2005; Li et al. 2004). In addition, some authors have considered MN PICs and plateau potentials as key mechanisms involved in the production of large extra forces observed after percutaneous electrical stimulations of muscles or tendon vibration (Collins 2007; Collins et al. 2001, 2002; Dean et al. 2007; Magalhaes and Kohn 2010; Nickolls et al. 2004). However, the mechanisms behind the extra forces have been a matter of debate in the experimental literature.

A recent study by Frigon and colleagues (2011) suggested that extra forces in response to electrical stimulation might mainly be attributed to peripheral mechanisms (*e.g.*, post-tetanic potentiation and phosphorylation of regulatory myosin light chains) and not to central mechanisms (*i.e.* PICs and plateaus). However, Collins and Bergquist (2011) argued that the assertion of peripheral mechanisms accounting for the extra torques observed by Frigon and colleagues (2011) only applied to muscle lengths that were shorter than those typically used in human experiments. Additionally, a recent study showed that a similar pattern of extra torque could be generated by applying both electrical muscle stimulation and tendon vibration (Magalhaes and Kohn 2010) accompanied by an increased motoneuronal excitability after tendon vibration. Other experimental findings have also advocated in favor of the involvement of PICs in the genesis of extra forces, suggesting that at least in part this motor behavior is plausible to have a central origin. For instance, Klakowicz et al. (2006) and Bergquist et al. (2011) showed an increase in H-reflex following a high-frequency electrical stimulation either in the muscle or in the peripheral nerve trunk.

In this study, the aim was to evaluate the effects of PICs on force generation using a stochastic neuromuscular simulator of the human leg, which is available in the internet

(Cisi and Kohn 2008). One objective was to verify if extra forces could be generated in the simulated neuromuscular system under conditions similar to those used in human experiments (Collins et al. 2001, 2002; Magalhaes and Kohn 2010). Two types of MN models were compared as to their collective actions in a MN pool over the generation of force: model with passive dendrite (PD) and model with an active dendrite (AD), containing a Ca^{++} PIC channel. Another objective was to study the properties of the extra-forces generated by a muscle under the control of the pool of MNs with AD models when compared with the forces generated when the pool had PD MN models. Particularly, the force variability was compared for the two types of MN pools. Finally, the effect of inhibitory inputs on the PIC was evaluated in a paradigm of fast force development, since inhibition is thought to modulate the PIC activity during normal motor behavior (Bennett et al. 1998; Hyngstrom et al. 2007; Hyngstrom et al. 2008; Johnson and Heckman 2010; Kuo et al. 2003). Part of this work was previously published in an abstract form (Elias and Kohn 2010).

2 Methods

The present study was performed using a neuromuscular simulator available in the internet in a downloadable version (the one used here) and also as an interactive system (Cisi and Kohn 2008; <http://remoto.leb.usp.br>). The general structure of the simulator was kept the same as the original, but an L-type Ca^{++} channel, responsible for a PIC, was included in the dendritic compartment of each MN model (see the mathematical description below).

In this study, some elements present in the simulator, *e.g.* Renshaw cells, Ia and Ib interneuron models, were not considered. We have constrained the neuromuscular model to a straightforward architecture (Fig. 1), representing the activation of the Soleus (SOL), Medial Gastrocnemius (MG), Lateral Gastrocnemius (LG), and Tibialis Anterior (TA) muscles by their associated MN pools. By convenience, mathematical models and their parameters were adopted the same for all motor nuclei, but the number of elements (MUs) varied for each muscle type (see the Appendix). Each MN pool was driven by independently activated stochastic point processes, which aimed to mimic either a sensory influx evoked by tendon vibration or a volitional descending command (Fig. 1(a)). A spike train generated by a given MN model activates, with a time delay depending on the axonal conduction velocity of the efferent fiber, a muscle unit that generates motor unit (MU) twitches and motor unit action potentials (MUAPs). The sums of twitches and MUAPs from all MUs of a given muscle result in the muscle force (F) and the EMG, respectively (Fig. 1(a) and (b)). A more detailed description of the system structure can be found elsewhere (Cisi and Kohn 2008).

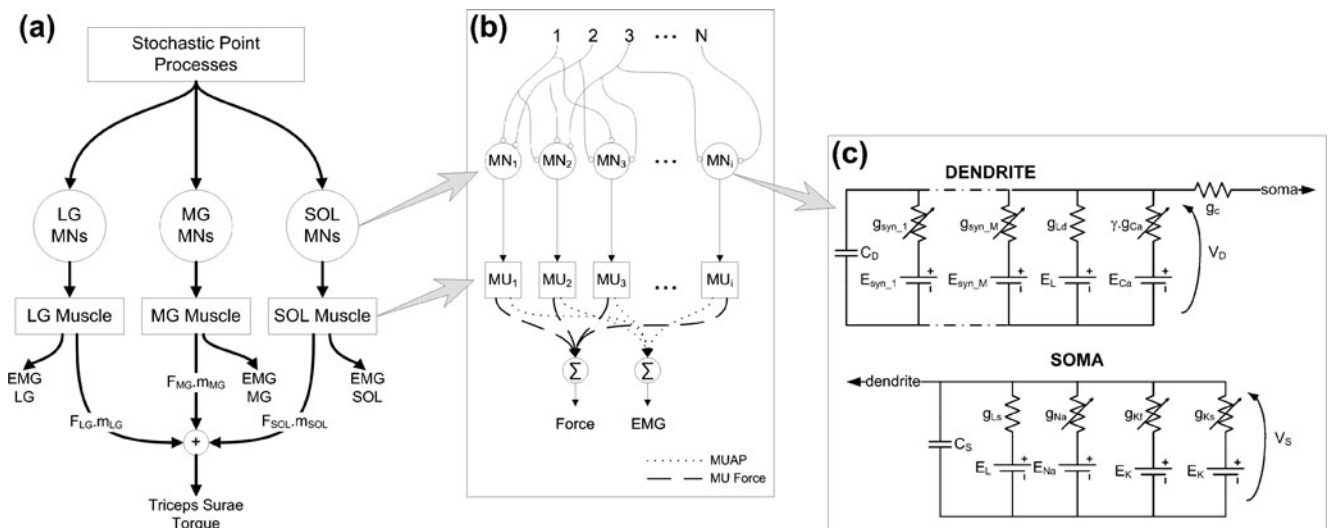


Fig. 1 General structure of the simulator used in this study. (a) Expanded view of the TS muscle group and its neural, muscular and biomechanical elements. (b) Detailed view of muscle-specific MUs. Each MU (motoneuron and its respective muscle unit) receives a

fraction of the stochastic inputs and generates twitches and MUAPs that summed produce the force and EMG, respectively. (c) Equivalent circuit used to represent each MN model. Symbols are defined in the Methods

2.1 Mathematical description

2.1.1 Motoneuron pool model

Within a motor nucleus, each type-specified (*i.e.*, S-, FR-, and FF-type) MN model was characterized by two compartments representing the soma and an equivalent dendrite. The corresponding electrical circuit is shown in Fig. 1(c) indicating the modeled ionic channels. The axon was simply associated with a conduction velocity (varying along the pool), which causes a delay of the MN action potentials to reach the muscle unit (the distance between the MN pool and the muscles was equal to 0.66 m). In each compartment, Equation (1) describes the membrane potential time course, with x representing the evaluated compartment (*i.e.*, soma or dendrite) and y the adjacent compartment (*i.e.*, dendrite when the evaluated compartment is the soma or soma when the evaluated compartment is the dendrite); C_x is the membrane capacitance (in nF); $g_{L,x}$ is the leakage conductance (in μ S); g_c is the coupling conductance (in μ S); E_L is the leakage Nernst potential (equal to the resting potential, in mV); $I_{ion,x}$ is the voltage-gated ionic current (in nA); and $I_{syn,x}$ is the synaptic current (in nA). The Appendix shows the equations used to calculate the passive elements with respect to the MNs’ geometric and electrotonic parameters.

$$\dot{V}_x(t) = -\frac{1}{C_x} \{g_{L,x}[E_L - V_x(t)] + g_c[V_x(t) - V_y(t)] + I_{ion,x}(t) + I_{syn,x}(t)\} \tag{1}$$

The somatic compartment comprised voltage-gated Na⁺ and fast K⁺ ionic channels, responsible for the genesis of

action potentials (spikes), along with a slow voltage-gated K⁺ channel, responsible for the afterhyperpolarization (AHP). Equation (2) represents the somatic voltage-gated ionic current ($I_{ion,s}$), in which \bar{g}_{Na} , \bar{g}_{Kf} , and \bar{g}_{Ks} are the maximal ionic conductances (in mS/cm²); E_{Na} and E_K are Na⁺ and K⁺ equilibrium potentials (in mV), respectively; $m(t)$, $n(t)$, and $q(t)$ are state variables for Na⁺, fast K⁺, and slow K⁺ channel activations, respectively; and $h(t)$ is the state variable for the Na⁺ channel inactivation.

$$I_{ion,s}(t) = \bar{g}_{Na}m^3(t)h(t)[E_{Na} - V_S(t)] + \bar{g}_{Kf}n^4(t) \times [E_K - V_S(t)] + \bar{g}_{Ks}q^2(t)[E_K - V_S(t)] \tag{2}$$

In contrast to the original PD MN model proposed by Cisi and Kohn (2008), a recently developed AD MN model (Elias and Kohn 2010) was included in the simulator structure. In this model, a voltage-gated L-type Ca⁺⁺ channel located in the dendritic compartment was mathematically represented, yielding a PIC that is described by Equation (3), with \bar{g}_{Ca} the maximal ionic conductance (in mS/cm²); E_{Ca} the Ca⁺⁺ equilibrium potential (in mV); and $p(t)$ the state variable for the L-type Ca⁺⁺ channel activation. A dimensionless variable γ , ranging from 0 to 1, represents the level of neuromodulation imposed by the descending monoaminergic pathways (Heckman et al. 2005; Heckman et al. 2009), with 0 meaning no PIC and 1 representing 100 % of MN PIC level. Changing this value one can simulate the effect of different levels of neuromodulatory drive on the spinal cord, *e.g.* abolishing the PIC effects by setting $\gamma=0$. The latter will result in a PD MN model equal to that previously described in Cisi and Kohn

(2008), which is valid for anaesthetized animals. This model was parameterized so that high values of γ (e.g., $\gamma \geq 0.80$) exhibit dynamics equivalent to cat MNs subject to a high level of neuromodulatory drive (Heckman and Lee 1999), whereas lower values ($\gamma \leq 0.60$) exhibit dynamics that are compatible with cat MNs for a medium-to-low neuromodulatory drive. In the present study, human MNs with a high neuromodulatory level are associated with $\gamma = 0.60$, which results in single MN firing rates compatible with those obtained from humans.

$$I_{ion,D}(t) = \gamma \{ \overline{g_{Ca}} p(t) [E_{Ca} - V_D(t)] \} \tag{3}$$

The state variables (m , h , n , q , and p) were described following the pulse-based formalism proposed by Destexhe (1997). Briefly, the first-order differential equations, in the form $\dot{\varphi} = \alpha_{\varphi}(1 - \varphi) - \beta_{\varphi}\varphi$ (with φ corresponding to a given state variable), can be analytically solved since the time course of forward and backward rates (α_{φ} and β_{φ}) were approximated by rectangular pulses, triggered when the membrane potential crosses a given threshold. When the threshold is crossed, these rectangular pulses turn on and remain active during a given time duration. While the pulse is on, Equation (4) and Equation (5) give the time course of activation (m , n , q , and p) and inactivation (h) variables, respectively. In these equations, α_{φ} and β_{φ} are forward and backward rate constants, respectively; t_{on} is the time at pulse activation, and φ_a^0 and φ_i^0 are the values of $\varphi_a(t)$ and $\varphi_i(t)$ at that time. The membrane threshold and pulse duration are different for somatic and dendritic channels. In somatic channels, the membrane threshold (V_{th}) is equal to the value of spike threshold, which is given by the product between the rheobase current and the motoneuron input resistance (Cisi and Kohn 2008). The pulse duration for the somatic channels is equal to 0.60 ms. The dendritic Ca^{++} channel had a membrane threshold similar to the PIC threshold (V_{th-Ca}) that was reported in the experimental literature for decerebrate cats (Kiehn and Eken 1998; Lee and Heckman 1998a, 1999; Schwindt and Crill 1980a); the pulse, once activated, remains active while the membrane potential is higher than V_{th-Ca} .

$$\varphi_a(t) = \varphi_a^0 e^{-\beta_{\varphi}(t-t_{on})} \quad t_{on} < t \leq t_{off} \tag{4}$$

$$\varphi_i(t) = 1 + (\varphi_i^0 - 1) e^{-\alpha_{\varphi}(t-t_{on})} \quad t_{on} < t \leq t_{off} \tag{5}$$

Before and after the pulse, Equation (6) and Equation (7) give the time course of activation and inactivation variables, respectively. In these equations, α_{φ} and β_{φ} are forward and backward rate constants, respectively; t_{off} is the time at pulse

deactivation, and φ_a^0 and φ_i^0 are the values of $\varphi_a(t)$ and $\varphi_i(t)$ at that time.

$$\varphi_a(t) = 1 + (\varphi_a^0 - 1) e^{-\alpha_{\varphi}(t-t_{off})} \quad t \leq t_{on} \text{ and } t > t_{off} \tag{6}$$

$$\varphi_i(t) = \varphi_i^0 e^{-\beta_{\varphi}(t-t_{off})} \quad t \leq t_{on} \text{ and } t > t_{off} \tag{7}$$

Almost all voltage-gated ionic channel parameters had a piece-wise linear variation along the MN pool (Table 1). The somatic parameters were chosen so that behaviors of a single PD model match experimental results from type-specified MNs of anaesthetized cats (e.g., AHP amplitude, AHP duration, and f-I curves). In addition, the dendritic channel was parameterized so that behaviors of a single AD model match experimental data from partially- and fully-bistable MNs of decerebrate cats (Bennett et al. 1998; Heckman and Lee 1999; Lee and Heckman 1998a, b, 1999). Figure 2 shows an example of input–output functions from a single AD MN model. The resulting f-I curve (Fig. 2(a)) of the AD MN model ($\gamma = 0.60$) had a gain of 2.80 Hz/nA (40 % higher than the corresponding PD MN model), which is compatible with experimental data reported in the literature (Bennett et al. 1998; Lee and

Table 1 Parameter values adopted in the modeling of voltage-gated ionic channels of S-, FR-, and FF-type MN models. The range of values is provided (with a linear distribution), except for those parameters that were maintained constant along the pool

Parameter	Unit	Value			
		S-type	FR-type	FF-type	
Soma	$\overline{g_{Na}}$	mS/cm ²	30	30	30
	$\overline{g_{Kf}}$	mS/cm ²	4	4–2.25	2.25–0.50
	$\overline{g_{Ks}}$	mS/cm ²	16–25	25–19	19–4
	E_{Na}^a	mV	120	120	120
	E_K^a	mV	–10	–10	–10
	α_M	ms ^{–1}	22	22	22
	β_M	ms ^{–1}	13	13	13
	α_H	ms ^{–1}	0.50	0.50–11.25	11.25–22
	β_H	ms ^{–1}	4	4–13	13–22
	α_N	ms ^{–1}	1.50	1.50–11.75	11.75–22
Dendrite	β_N	ms ^{–1}	0.10	0.10–11.05	11.05–22
	α_Q	ms ^{–1}	1.50	1.50–11.75	11.75–22
	β_Q	ms ^{–1}	0.025–0.038	0.038–11.025	11.025–22
	$\overline{g_{Ca}}$	mS/cm ²	0.038–0.029	0.029–0.016	0.016–0.012
	E_{Ca}^a	mV	140	140	140
	α_P	ms ^{–1}	0.008	0.008	0.008
	β_P	ms ^{–1}	0.014–0.016	0.016–0.019	0.019–0.020
	V_{th-Ca}^b	mV	–5.20––4.40	–4.40––4.20	–4.20––4.00

^a With reference to the resting potential. ^b With reference to the spike voltage threshold (V_{th}). V_{th-Ca} values were chosen randomly (CV= 0.01) around the means

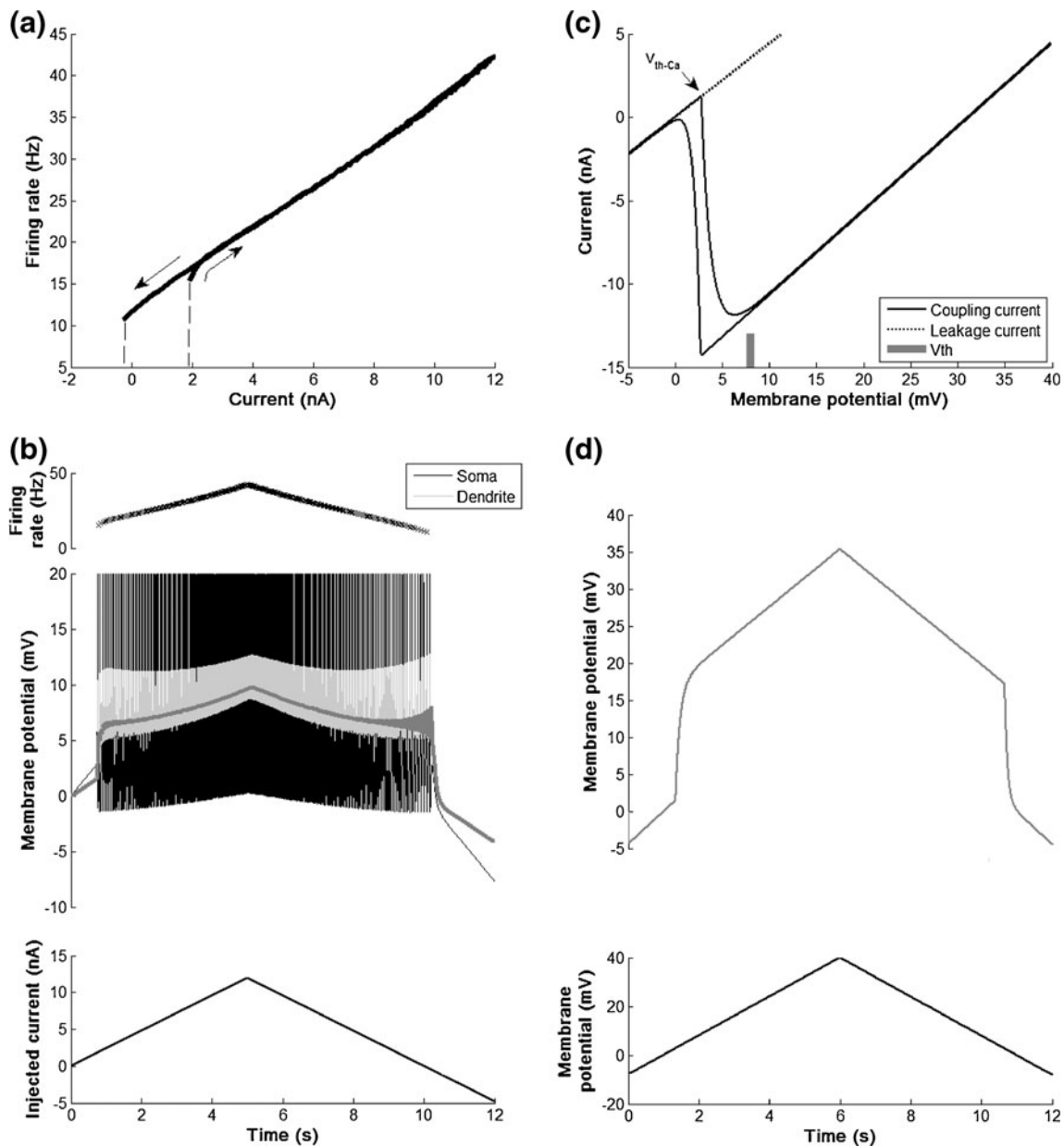


Fig. 2 Single active dendrite (AD) MN model ($\gamma=0.60$) input–output relations. **(a)** Frequency-to-current (f-I) curve. The arrows indicate the rising and falling phases of the firing rate values in response to a slow triangular current injected into the soma. Dashed vertical lines indicate the recruitment and derecruitment current values. **(b)** Bottom: Triangular current injected into the soma. Middle: Somatic (black) and dendritic (light gray) membrane potentials. The somatic spikes were clipped at 20 mV. The dark gray curve represents the lowpass-filtered dendritic membrane potential (2 Hz cutoff frequency), showing the

onset of a dendritic plateau after MN recruitment. Top: Instantaneous firing rate. **(c)** Current-to-voltage (I-V) curve during a voltage-clamp simulation. Only the coupling current was measured to quantify the PIC (maximum PIC amplitude was measured after the subtraction of the leakage current). The vertical grey bar indicates the spike threshold (V_{th}) and the arrow indicates the PIC onset (V_{th-Ca}). **(d)** Bottom: Clamped somatic membrane potential. Top: Resulting dendritic membrane potential.

Heckman 1998b). It is worth noting the difference between recruitment and derecruitment current values (dashed vertical lines in Fig. 2(a)), which is characteristic of bistable MNs. The hysteresis in the f-I curve is due to the difference in the currents needed to turn-on and turn-off the PIC. The latter is evidenced by the hyperpolarized membrane potential that turned-off the dendritic plateau potential (middle

panel of Fig. 2(b)) and, hence, derecruited the neuron. The I-V curve (Fig. 2(c)) was estimated by voltage-clamping the soma (bottom panel in Fig. 2(d)) and the PIC was measured as the coupling current between soma and dendrite (*i.e.*, the current arriving in the soma). This input–output relation had a classic N-shape characteristic due to PIC activation in the dendrite (Schwindt and Crill 1980a,b; Lee and Heckman

1998a) and the PIC amplitude (15.04 nA) was within the experimental range reported in the literature (Lee and Heckman 1998a, 1999).

Synaptic conductances were modeled by the kinetic model proposed by Destexhe and colleagues (1994). The synaptic current was given by the sum of all excitatory (N_e) and inhibitory (N_i) synapses arriving onto a given compartment (Equation 8). In this equation, $g_e(t)$ and $g_i(t)$ characterize the excitatory and inhibitory conductances, respectively; E_e and E_i are the reversal potentials for excitatory and inhibitory synapses, respectively. The values of maximal conductances were 600 nS and 500 nS for excitatory and inhibitory synapses, respectively, and the reversal potentials were 70 mV and -16 mV (both with respect to the resting potential) for excitatory and inhibitory synapses, respectively. These values were adopted so that individual excitatory post-synaptic potentials (EPSPs) and inhibitory post-synaptic potentials (IPSPs) matched experimental results (Finkel and Redman 1983; Stuart and Redman 1990). In order to reduce the computational load required to represent a complex neuronal network, the algorithm proposed by Lytton (1996) was used to account for the effects of multiple synaptic inputs to a given MN.

$$I_{syn,x}(t) = \sum_0^{N_e} g_e(t)[V_x(t) - E_e] + \sum_0^{N_i} g_i(t)[V_x(t) - E_i] \quad (8)$$

2.1.2 Torque and electromyogram models

The MU twitch model was the discrete-time impulse response of a second-order critically-damped system (Fuglevand et al. 1993; Cisi and Kohn 2008), which was described by Equation (9), with A_{peak} the twitch amplitude (in N); t_{peak} the twitch contraction time (in ms); T the time step (in ms); and $e(n)$ the discrete-time spike train. The MU twitch parameters were based on human data and had a piece-wise linear variation along the pool (see Table 2). Individual muscle force (F) was given by the sum of all MU twitches and the torque due to each muscle was

calculated by multiplying F and the muscle's moment arm (m)—4.13 cm for SOL; 4.18 cm for MG; 4.29 cm for LG; and 3.70 cm for TA (Menegaldo et al. 2004). Positive torque was defined in the plantarflexion direction (torque generated by the TS—see Fig. 1(a)), whereas negative torque was due to the TA contraction (dorsiflexion).

$$F(n) = 2e\left(\frac{-T}{t_{peak}}\right)F(n-1) - e\left(\frac{-2T}{t_{peak}}\right)F(n-2) + \frac{A_{peak}T^2}{t_{peak}}e\left(1-\frac{T}{t_{peak}}\right)e(n-1) \quad (9)$$

The MUAPs were described by first- and second-order Hermite-Rodriguez functions (Cisi and Kohn 2008; Zhou and Rymer 2004) that are described by Equations (10) and (11), respectively, with A_M the scale factor; λ_M the time factor; t_{spike} the arrival time of a spike; and $u(t)$ the step function. Each MU of a pool randomly received a biphasic (Equation 10) or triphasic (Equation 11) MUAP and the scale and time factors had a piece-wise variation along the pool (see Table 2). A spatio-temporal filtering of MUAPs was performed to represent the amplitude attenuation and increased duration of MUs located farther from the recording surface electrodes (Fuglevand et al. 1993; Cisi and Kohn 2008).

$$HR_1(t) = A_M(t - t_{spike})e^{-\left(\frac{t-t_{spike}}{\lambda_M}\right)^2}u(t - t_{spike}) \quad (10)$$

$$HR_2(t) = A_M\left[1 - 2\left(\frac{t - t_{spike}}{\lambda_M}\right)^2\right]e^{-\left(\frac{t-t_{spike}}{\lambda_M}\right)^2}u(t - t_{spike}) \quad (11)$$

2.2 Simulation protocols

All simulations were performed using a fourth-order Runge–Kutta integration method with a 0.05 ms time step.

2.2.1 Force versus intensity curve

A linearly rising current (ramp) was slowly injected into the MNs' soma to gradually recruit the motor pool of SOL muscle. The current intensity varied from 0 to 10 nA in 10 s, so that the muscle force could reach approximately 80 % of its maximum value (F_{max}). Four levels of neuromodulatory drive (γ) were evaluated: *i*) high, $\gamma=0.60$; *ii*) medium, $\gamma=0.30$; *iii*) low, $\gamma=0.15$; and *iv*) absent, $\gamma=0$. This protocol was useful to assess the effect of neuromodulatory level on the recruitment of a MN pool (Heckman et al. 2009).

Table 2 Range of values (linear interpolation between minimum and maximum values) adopted for the parameter values of motor unit twitches and motor unit action potentials (MUAPs)

Parameter	Unit	Value		
		S-type MU	FR-type MU	FF-type MU
A_{peak}	N	0.103–0.123	0.123–0.294	0.294–0.491
t_{peak}	ms	110.0–100.0	73.50–55.50	82.30–56.90
A_M	mV	0.105–0.125	0.125–0.300	0.30–0.50
λ_M	ms	0.80–0.70	0.70–0.60	0.60–0.50

2.2.2 Force variability

In this simulation protocol, the neuromodulation level (γ) of the MN pool was varied from zero (passive network) to 0.60 (high neuromodulatory activity) in order to evaluate its effect on the force variability. To evoke a maintained force level around 20 % F_{\max} , the SOL MN pool was driven by 100 independent input spike trains, each following a homogeneous Poisson point process. The mean rate of each process was in the range from 160 Hz to 34 Hz for γ values varying from 0 to 0.60. Any trend in force caused by the late recruitment of MNs was removed before data analysis. Force variability was measured as mean (μ_F), standard deviation (σ_F), and CV ($CV_F = \sigma_F / \mu_F$) of the last 5 s of the force time course, which was previously filtered using a lowpass fourth-order Butterworth filter with a 20 Hz cutoff frequency.

2.2.3 Torque plateau

This protocol was performed on the TS (SOL+MG+LG) muscle. The neuromodulatory level of the MN pool was absent (PD MN models) or high (AD MN models with $\gamma = 0.60$) in independent simulations. Poisson point processes (100 independent parallel inputs), representing the collective inputs to the MN pools, maintained a basal torque (BT) of approximately 5 % of the maximum torque (MT) with a 30 % connectivity in each motor pool (*i.e.*, each input Poisson process activated only 30 % of the MNs of the pool, chosen at random for each input). The intensity of the Poisson point processes used to maintain the BT was larger in the passive network in comparison with the active network, since AD MN models have an increased excitability due to the PIC, hence requiring smaller currents of synaptic origin to achieve the same firing rate of a PD MN model. After the first 2 s of simulation, the input point processes were switched to nonhomogeneous Poisson processes with mean rates modulated by 2 s duration and 15 Hz amplitude pulses (shown at the bottom panel in Fig. 5(a)). The BT was calculated between 1 and 2 s of simulation, whereas the extra torque (ET) was calculated as the difference between the torques measured in the last second of each inter-pulse interval and the BT (shadowed areas at the top panel of Fig. 5(a)). This protocol is similar to those that used either electrical stimulation or tendon vibration in human and cat experiments (Collins 2007; Collins et al. 2001, 2002; Dean et al. 2007; Frigon et al. 2011; Magalhaes and Kohn 2010; Nickolls et al. 2004).

2.2.4 Torque and EMG hysteresis

The same muscle group as well as the neuromodulatory level (*i.e.* absent or high) of the preceding section (2.2.3)

was used in these simulations. A BT ~ 2 % MT was maintained by 100 Poisson point processes (similarly to 2.2.3, the Poisson intensity was lower in the AD network than in the PD network), and a slow 15 Hz amplitude triangular-shaped modulation of the intensities of the stochastic point processes was performed between 2 and 22 s (see bottom panels on Fig. 6). Individual muscle EMG signals were full-wave rectified and filtered using a lowpass fourth-order Butterworth filter (6 Hz cutoff frequency). Relationships between the plantarflexion torque *versus* input modulation and the EMG envelope *versus* input modulation were obtained for both passive ($\gamma = 0$) and active ($\gamma = 0.60$) networks. This protocol is also similar to those used in human and cat experiments using either electrical stimulation or tendon vibration (Collins 2007; Collins et al. 2001, 2002; Dean et al. 2007; Frigon et al. 2011; Magalhaes and Kohn 2010; Nickolls et al. 2004).

2.2.5 Effects of inhibitory inputs on torque control

The objective of these simulation experiments was to study the effect on the torque level of a purely inhibitory input to the MN pool when PICs were being generated. This effect was compared to that obtained by generating a counterbalancing dorsiflexion torque by the activation of the TA muscle model. First, a phasic plantarflexion torque was generated by a 1.25 s duration excitatory input followed by a 500 ms inhibitory input to the plantarflexor pool. At the end of the excitatory input (concomitant to inhibition onset), a 1 s excitatory input was imposed on the dorsiflexor pool. Another simulation was performed with both plantar and dorsiflexor excitation but without inhibition of the plantarflexor pool. Excitatory inputs were driven by 100 independent Poisson point processes with mean rate equal to 40 Hz, which was sufficient to generate a low torque, mimicking a low-amplitude phasic torque. The inhibitory input was driven by 100 independent Poisson point processes with the mean rate equal to 100 Hz, which was sufficient to turn off the MN PICs. Plantarflexion and dorsiflexion torques were calculated individually and the resultant torque was given by the linear difference between both torques. In addition, raw EMGs of the SOL and TA were calculated.

3 Results

The inclusion of a dendritic Ca^{++} PIC in each single MN model greatly changed the dependence of the simulated muscle force on the slowly rising injected current (Fig. 3). Both recruitment threshold (minimal injected current that generated force—see arrows in Fig. 3) and gain (slope of the linear region of the curve) of the motor pool input–output relationship were modified by the neuromodulation level,

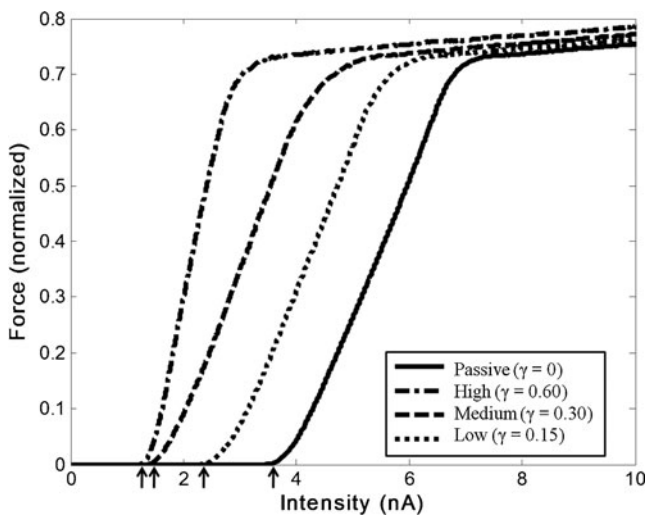


Fig. 3 Input–output functions of the SOL motor pool for different levels of monoaminergic drive (γ). The input was a slowly increasing current and the calculated output was the resultant muscle force normalized with respect to the maximal value for that muscle (F_{max}). Arrows indicate the recruitment threshold for each curve (minimal current sufficient to generate force). The gain was defined as the slope of the linear region of each curve

with a more pronounced effect on gain observed for high levels (dash-dotted curve in Fig. 3). However, large changes in force recruitment were noticed even for low levels of neuromodulatory activity. For instance, there was a 70 % reduction in the recruitment threshold of an active network with low neuromodulation level (dotted curve in Fig. 3) when compared with a purely passive network (solid curve in Fig. 3). For values $\gamma \geq 0.30$, the recruitment threshold was not significantly changed and major changes were in the gain (dashed and the dash-dotted curves in Fig. 3).

The neuromodulatory activity had also a remarkable effect on force variability (Fig. 4). Force CV varied little when passing from a passive dendrite condition to an active one with small or medium neuromodulation levels. However, for a higher neuromodulation level the force standard deviation (bottom of Fig. 4) and CV were considerably reduced. For a similar mean force (~ 18 % of the maximum muscle force), the CV_F for $\gamma=0.60$ was approximately 3 times lower than the value obtained for $\gamma=0$, whereas the value for $\gamma=0.30$ was just slightly lower (~ 15 %) than that of the passive condition.

3.1 Extra torque and torque hysteresis

Figure 5(a) shows the torque evoked in the TS muscle by 2 s duration pulse-shaped variations of the input stochastic point process mean rates. Before the first pulse, the mean BT was adjusted to be approximately equal in both passive and active networks (~ 5 % MT). When the mean rate (intensity) of the Poisson point processes was raised by

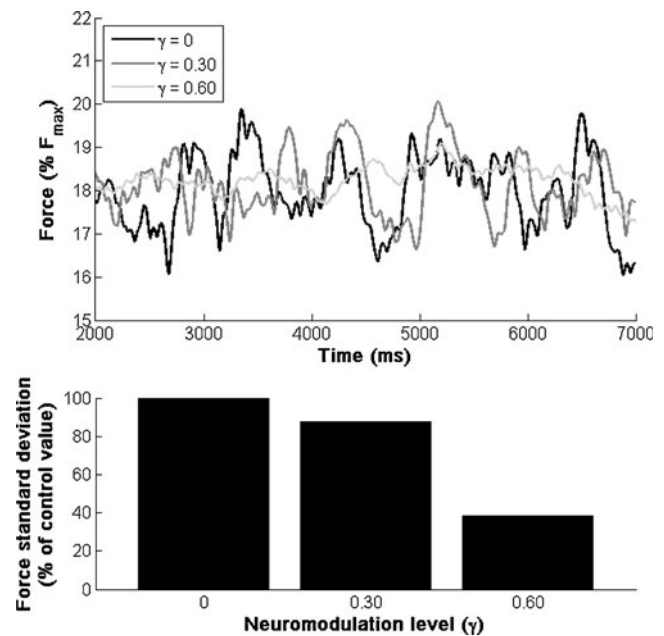
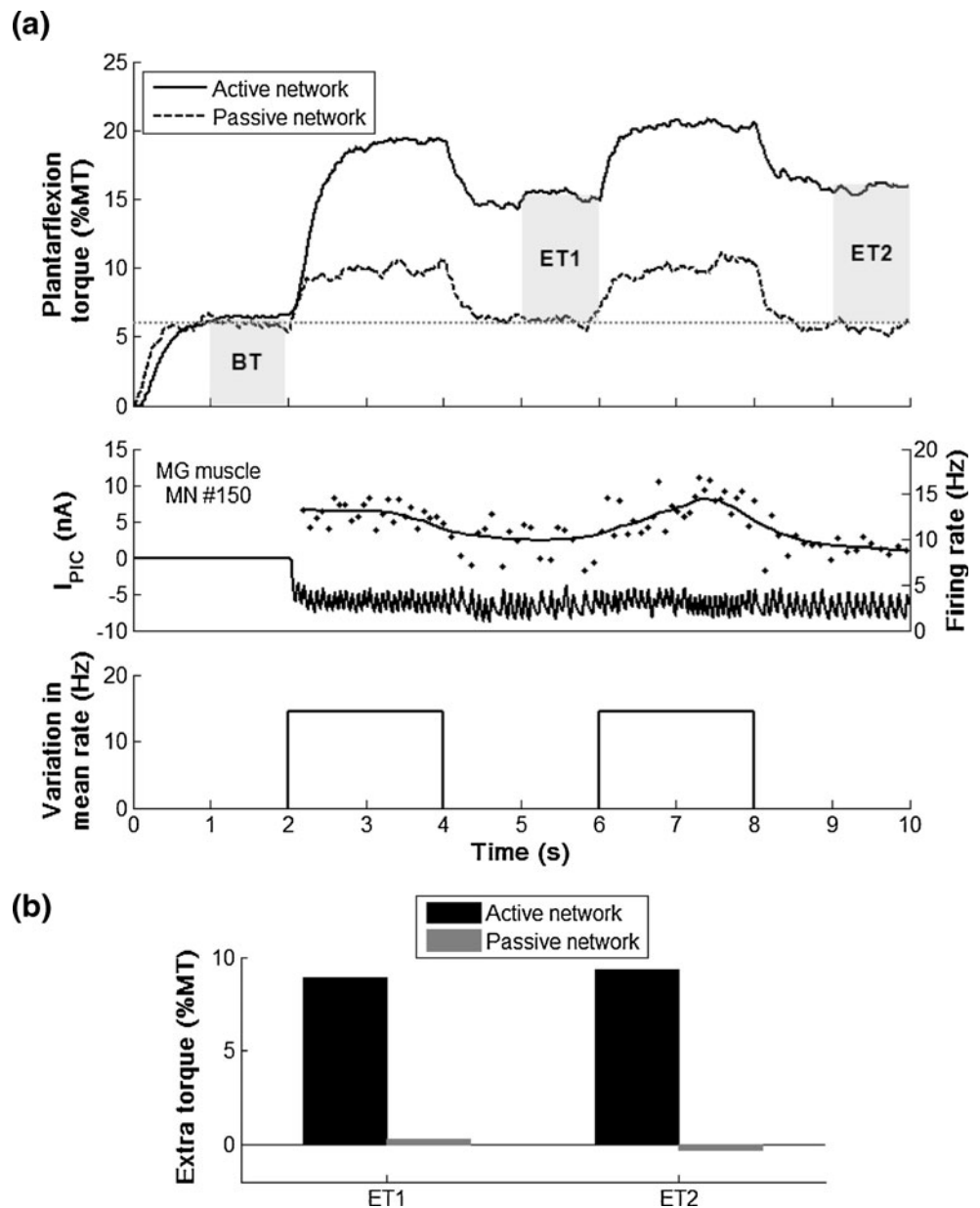


Fig. 4 Force variability analysis. Top: Time course of force for different levels of neuromodulatory drive. Bottom: Force standard deviation (σ_F) as a function of the neuromodulation level. The control value was adopted when the neuromodulation was absent (*i.e.*, passive network)

15 Hz both the passive and active networks showed an increase in muscle torque, with a more pronounced effect in the active network (continuous line). At the end of the pulse the TS torque of the passive network (dashed line) returned to a value similar to the BT, indicating that a negligible ET was evoked by the neuronal circuitry. Conversely, the active network showed a long-lasting plateau-like torque, which is much higher than BT (Fig. 5 (b)). This ET was generated by the self-sustained discharge of some MNs that kept discharging after the pulse (middle panel shows the firing rate of MN #150 from the MG motor nucleus). A second pulse was delivered to evaluate the “warm-up” effect of the PIC (Fuglevand et al. 2006). Again, the passive network did not show any ET, whereas the active network had an ET very close to the first (compare the ET1 and ET2 in Fig. 5(b)), indicating that no significant “warm-up” effect was present in this simulation (see the PIC time course of a single MN in the middle panel of Fig. 5(a)). The values of ET obtained (~ 10 % MT) were similar to the experimental results from humans reported previously in the literature, *e.g.*, Magalhaes and Kohn (2010).

When the input was slowly modulated by a triangular-shaped function the TS torque generated by the active network showed a clear counterclockwise hysteresis (Fig. 6(a) solid line), similar to that frequently recorded in humans after percutaneous electrical stimulation (Collins et al. 2002). Conversely, the TS torque generated by the

Fig. 5 Torque plateau and measured extra torque (ET). (a) Bottom: variation in mean rate of Poisson point processes. The basal value (subtracted for better visualization) in both passive and active networks was adjusted (95.20 Hz in the passive and 18.20 Hz in the active network) in order to generate a basal torque (BT) of ~5 % MT. Middle: PIC time course (negative value means inward current) and instantaneous firing rate (black curve represents the moving average) of MN #150 of the MG muscle pool. Top: plantarflexion torques (normalized by the maximum torque, MT) calculated for the passive (dotted curve) and active (continuous curve) dendrite motoneuronal networks. Shaded areas indicate the evoked basal torque (BT) and the measured ETs (ET1 and ET2). (b) Measured ETs after the first (ET₁) and second (ET₂) pulses



passive network (Fig. 6(a) dotted line) did not show any hysteresis. Figure 6(b) shows the firing rate of three AD MN models of the SOL motor pool. All these neurons had a hysteresis in its discharge rate as a function of time, similar to that observed in f-I curves of single AD MNs (e.g., Fig. 2).

The information provided in Fig. 7 is unique to the simulations due to the challenge of recording the activity of hundreds to thousands of neurons from the human spinal cord. However, in the simulator these data are readily available and may serve for studies focused on how the muscle force was influenced by the MNs' discharges. The same input variation evoked a large force in the active network in comparison with the passive, as was previously assessed by the motor pool input–output curves (Fig. 3). This large

force can be explained by two factors: *i*) a large number of MNs were recruited in the active network (compare Fig. 7(a) and (b)) due to their increased sensitivity to excitatory inputs, *i.e.*, less excitatory synaptic current was sufficient to recruit more AD MNs; *ii*) due to their increased excitability the mean firing rate of AD MNs was somewhat higher than that of PD MNs (examples in Fig. 7(c) and (d)).

Figure 7(a) evidenced that the force (or torque) hysteresis associated with the active network was due to differences in recruitment and de-recruitment of MNs. For instance, the last recruited MN in the active network (MN #620) was recruited near the peak of the triangle, but once recruited it continued to discharge even with an excitatory current lower than that required for its recruitment. As an additional example, MN #246 in the active network was recruited

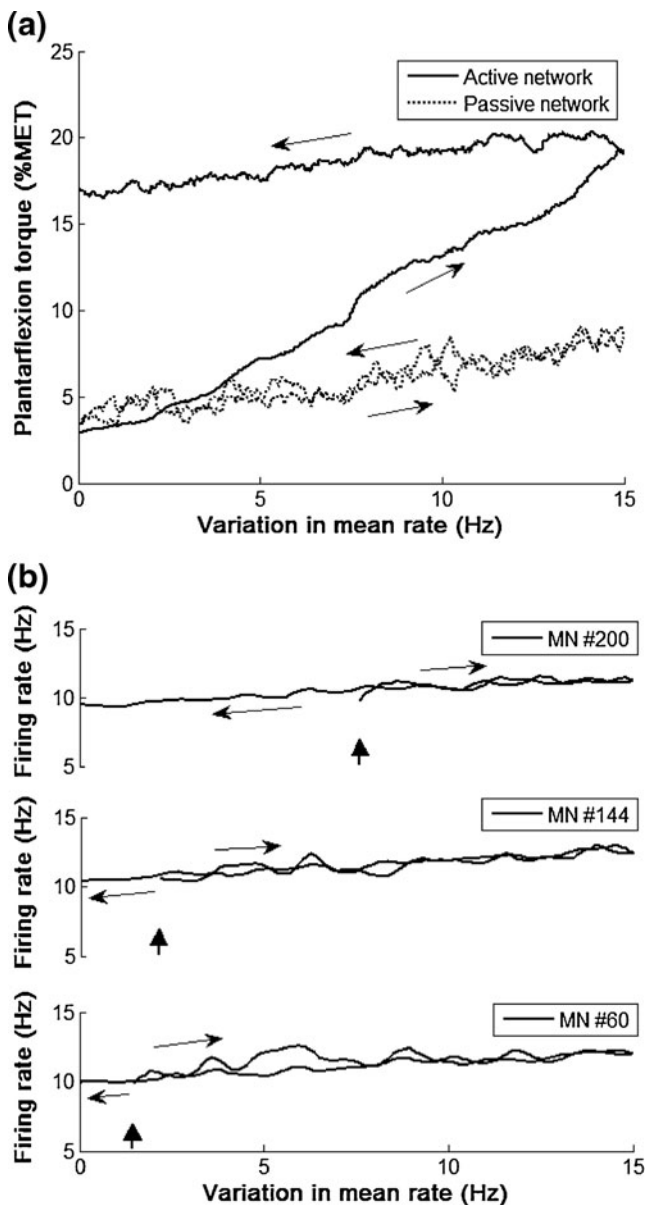


Fig. 6 (a) Relationship between plantarflexion torque and MN pool input modulation level (variations in input mean rate). When the input (Poisson point processes) mean rate was modulated by a slow triangular waveform with a 15 Hz peak value (arrows correspond to the rising and falling phases), the active network (solid curve, $\gamma = 0.60$) generated a marked hysteresis in torque, whereas no evident hysteresis was observed in the torque generated by the passive network (dotted curve). The input modulation had the same amplitude for both passive and active networks, but the basal value in each condition was adjusted (88.50 Hz in the passive and 16.70 Hz in the active network) so that the initial force had the same value in both situations. (b) Firing rate (moving average) for three MNs of the active network. The light arrows indicate the rising and falling phases of MN firing rate corresponding to the slow modulating triangular waveform. Vertical arrows indicate the recruitment of each MN

and de-recruited with different levels of synaptic input (Fig. 7(c)), whereas in the passive network (Fig. 7(d)) the recruitment and de-recruitment of the same MN was at an approximately

equal input level. These are typical features of self-sustained discharges evoked by PICs found in animal experiments (Bennett et al. 1998; Hounsgaard et al. 1988; Lee and Heckman 1996, 1998b).

We have also simulated the EMG of the TS muscle during the slow triangular modulation of the motor pool input. The results (Fig. 8) showed a similar pattern of hysteresis in the EMG envelope of the active network as was also found for the muscle torque. On the other hand, the neuromuscular system driven by the PD MN network did not present any marked hysteresis in the EMG (consistent with the torque findings). In both conditions (active and passive), the intensity (*e.g.*, power) of the EMG was higher for the SOL muscle in comparison with the gastrocnemii due to its relative importance in the TS. Similar data (unpublished) were experimentally recorded in our lab during triangular modulation of tendon (calcaneous) vibration in humans.

3.2 Effect of inhibitory inputs

This simulation emphasizes the importance of inhibitory inputs in a neuronal network functioning under the effect of PICs. In Fig. 9(a) TS excitation led to the generation of a torque (light gray curve) that remained relatively high even when the TS activation was turned off, due to the self-sustained discharge of MNs. An activation of the TA muscle (Fig. 9(a), dark gray curve) helped decrease the torque but this occurred quite slowly (Fig. 9(a), black curve) and with a high degree of co-contraction, limiting the execution of a phasic force. The TS and TA EMGs are seen below, indicating that the last interval was characterized by a co-contraction. On the other hand, in Fig. 9(b) the simultaneous activation of the TA muscle with inhibitory presynaptic spike trains to the TS MN pools led to a fast decay of the resultant torque (Fig. 9(b), black curve), since the self-sustained discharges of MNs in the TS motor pool were turned off by the inhibition. The respective EMGs are shown below and indicate that the TS activity was turned off when the TA muscle was activated.

4 Discussion

A stochastic and nonlinear neuromuscular simulator with parameters estimated from the biophysical literature was used to investigate the role of dendritic PICs on torque generation. The first result, shown in Fig. 3, exemplified the powerful effect exerted by PICs on the relation between muscle force and input current. Different motor outputs might be achieved by adjusting the level γ of neuromodulatory activity, adopted as equal for all MN types in a specific pool. A qualitatively analogous result was obtained by Heckman (1994) but with a very simplified MN pool

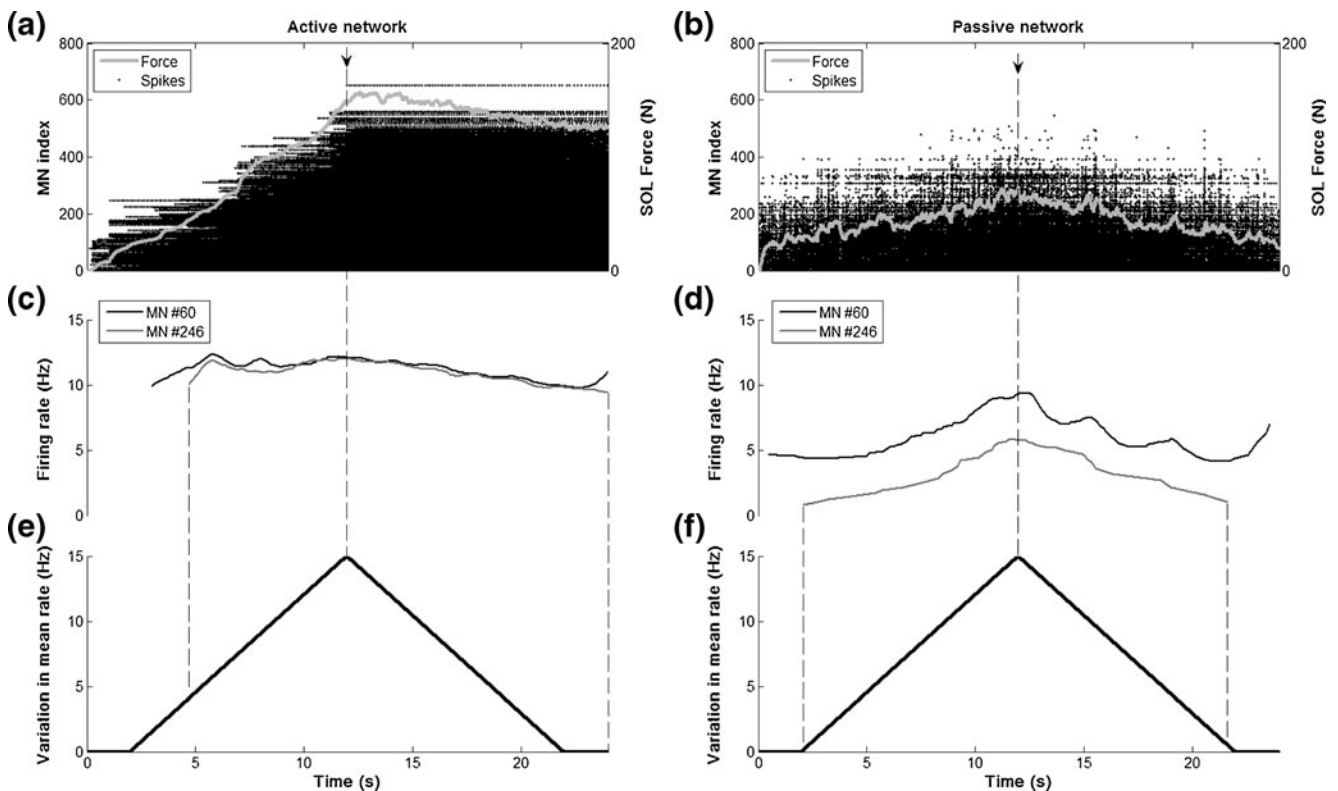


Fig. 7 The role of MN-pool self-sustained discharges on torque hysteresis. Left and right columns present the results for the AD ($\gamma = 0.60$) and PD MN networks ($\gamma = 0$), respectively. (a) and (b): Raster plots of

recruited MNs and the force generated by the SOL muscle (continuous line). (c) and (d): Firing rates (moving-average) of two representative MNs. (e) and (f): Input modulation signal

model of the feline MG muscle. The linear range of the input–output curve is related to the rate modulation of each recruited MN and reflects the cell’s frequency-to-current transduction (f-I curve). In cat MNs, the activation of PICs induces changes in both recruitment threshold and f-I gain (Bennett et al. 1998; Hounsgaard et al. 1988; Lee and Heckman 1996, 1998b). In our type-specified MN models, similar changes in f-I curves were observed (Fig. 2) and the motor output reported in Fig. 3 is an emergent behavior of the non-homogeneous neuronal network. The sigmoidal shape of these curves is due to saturation of individual MU forces that occurs at high intensity inputs. Technical challenges preclude the estimation of such a relation in both humans and animals (Heckman et al. 2009), which means that computational neuroscience techniques (as developed and used here) are the only tools capable of providing clues as to the relevant physiological parameters. Improvements in our models could be done, for example, by smoothing the sharp transitions in the rheobase curve between different MN types and/or decreasing the rheobase slopes for the F-type MNs. However, these refinements will probably have little impact on the predictions obtained from the results.

A noteworthy result of this study was the influence of the PIC on the force variability (Fig. 4). There was a remarkable

reduction in the σ_F for high neuromodulation levels when compared with lower levels. For low neuromodulation levels the force variability was quite similar to that of the passive network. This similarity may be due to the low number of bistable MNs for these conditions, regardless of the PIC activation along the pool. The PIC magnitude was lower (or absent) for $\gamma < 0.40$ and did not induce a profound change in MN model dynamic behavior, so that the interspike interval (ISI) variability, which in this study was reflected in the force variability, was also similar for these conditions. When a higher neuromodulatory activity was imposed on any given MU, the corresponding ISI variability and MU force variability were significantly decreased (unpublished data) because a smaller level of synaptic current was sufficient to recruit the MU, so that less synaptic variability was imposed onto the MN membrane. Decreased ISI variability was also shown in previous modeling studies when AD and PD MN models were compared (Taylor and Enoka 2004; Williams and Baker 2009). Actually, this result serves as a prediction, since, to the best of our knowledge, no experimental findings have been reported on this issue. From a functional perspective, this finding suggests that if the spinal cord were under the effect of a relatively large neuromodulatory activity, a steadier (less variable) force

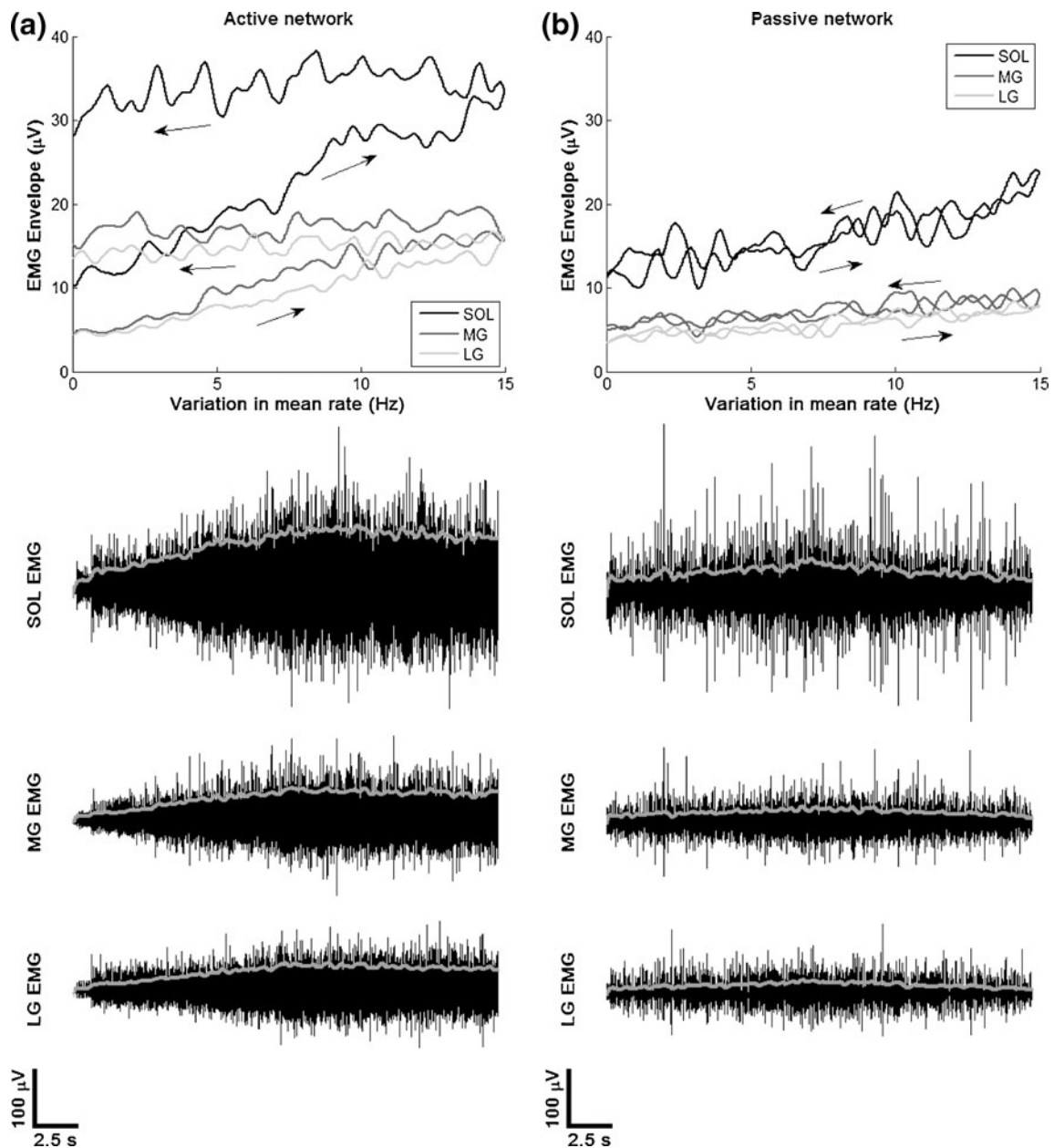


Fig. 8 Effect of PICs on EMG. (a) Active network ($\gamma = 0.60$) and (b) passive network ($\gamma = 0$). Top panel: relationship between EMG envelope and the input modulation. Arrows indicate the rising and falling regions of the triangular input (the same as in Figs. 6 and 7). Bottom

panel: raw EMG (black curves) of plantarflexors and the corresponding envelope (light gray curves, which were multiplied by 3 for better visualization)

would be developed, reinforcing the hypothesis that PICs may be useful during postural tasks (Gorassini et al. 1998; Heckman et al. 2009) and precision movements.

4.1 Effects of PICs on extra torque and torque hysteresis

Several studies on humans have discussed the importance of PICs on the genesis of torque plateau after percutaneous electrical stimulation or tendon vibration (Bergquist et al.

2011; Collins et al. 2001, 2002; Klakowicz et al. 2006; Magalhaes and Kohn 2010; Nickolls et al. 2004). These studies showed patterns of torque (force) that were reproduced by the simulator (Figs. 5 and 6), both with pulse and triangular modulation of the input. This suggests that the geneses of ET and torque hysteresis are entirely compatible with mechanisms of central origin, particularly the activation of motoneuronal PICs yielding plateau potentials. Increased F-wave amplitudes measured before and after

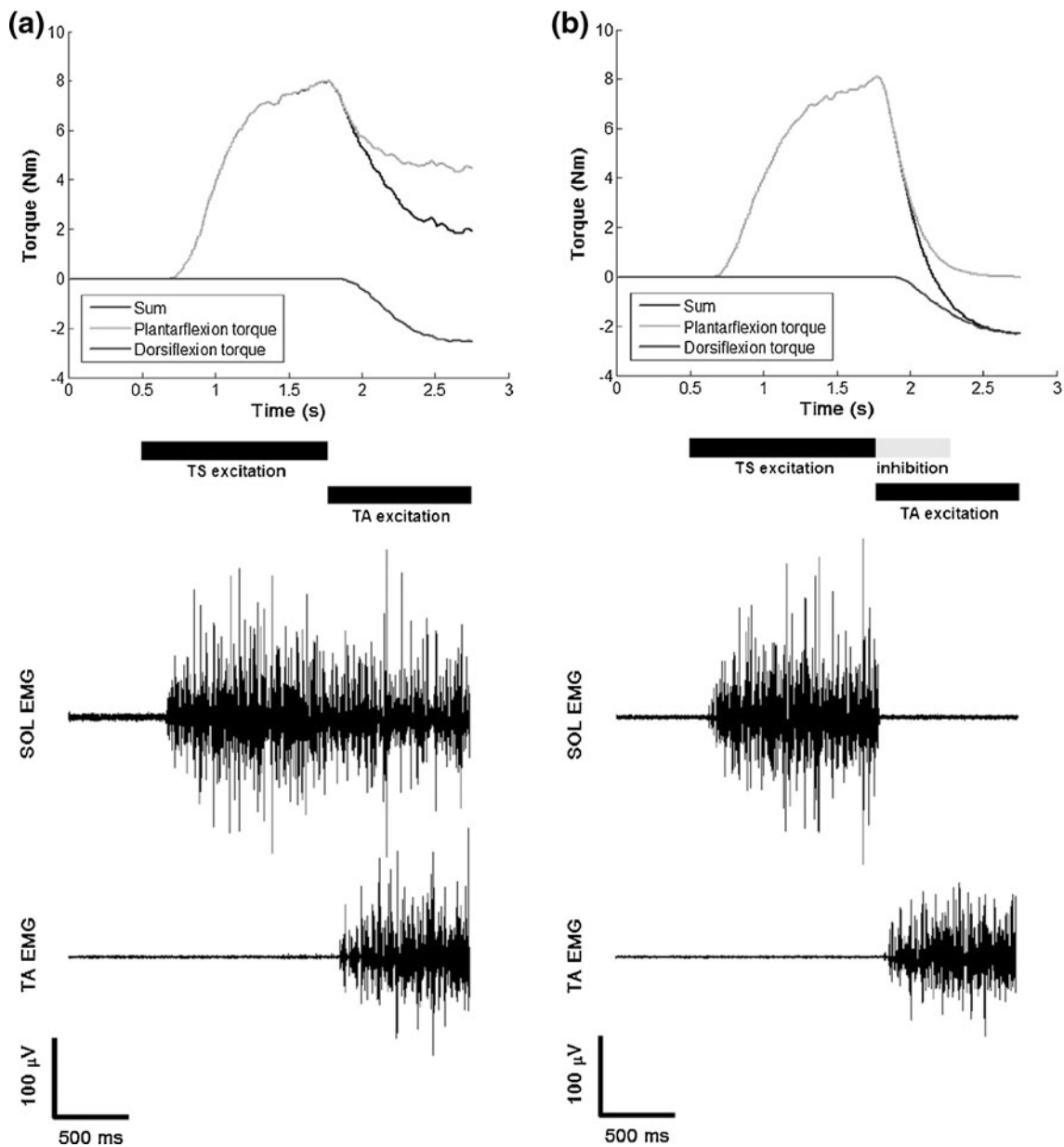


Fig. 9 Effect of an inhibitory input on resultant torque generation by both TS and TA muscle groups. TS MN pool without (a) and with (b) inhibition. Top: plantarflexion (light gray), dorsiflexion (dark gray), and the resulting torque (plantarflexion + dorsiflexion, black). Horizontal bars indicate the excitation of TS and TA, as well as the

inhibitory input delivered to the TS motoneuron pool (at right graph, grey horizontal bar). Bottom: Raw EMGs of SOL and TA muscles. Note the marked co-contraction of SOL and TA muscles in (a) but without achieving a fast force resetting to the resting value (black line in the upper panel)

tendon vibration were described in the literature (Magalhaes and Kohn 2010), suggesting that the motor pool excitability was augmented by vibration. A similar finding was reported by Klakowicz et al. (2006) and Bergquist et al. (2011) comparing H-reflex amplitudes before and after high-frequency electrical stimulation. Nevertheless, all these experimental studies did not exclude the role of other central mechanisms, such as synaptic post-tetanic potentiation (Lloyd 1949), and peripheral mechanisms, such as muscular

thixotropy, muscle post-tetanic potentiation, and phosphorylation of regulatory myosin light chains. A recent experimental work (Frigon et al. 2011) examined the involvement of PICs on the genesis of ET and stated that the previous results of Collins and co-workers (Collins et al. 2001, 2002; Klakowicz et al. 2006; Nickolls et al. 2004) using percutaneous electrical stimulation were merely due to intrinsic muscle properties. However, their results using tendon vibration, as also used in previous studies on cats (Hounsgaard et al.

1988), evoked plateau potentials in cat MNs and extra force (their Fig. 6). In response to this study, Collins and Bergquist (2011) argued that different experimental setups were used between the prior and recent studies, mainly concerning the joint angle (or muscle length) used by Frigon et al. (2011). Therefore, both central and peripheral mechanisms likely are involved in the genesis of extra force and force hysteresis in humans. In the present modeling and simulation study, PICs were shown to change properties of the spinal motoneuronal network generating conspicuous nonlinear motor behaviors, which are functionally important and have an impact in rehabilitation procedures (Bergquist et al. 2011; Dean et al. 2007; Magalhaes and Kohn 2010).

The inclusion of a dendritic Ca^{++} PIC profoundly changed the discharge properties of MNs in the spinal circuitry represented in the simulator. The ET (torque plateau) observed was due to the model's self-sustained discharge that lasted several seconds after an excitatory input. Silent MNs were recruited by an increased excitatory input (pulse modulation in Fig. 5) and continued to discharge even after the removal of the excitatory synaptic current. This "unexpected" discharge evoked by the PIC activation accounted for the observed phenomenon, and when PICs were removed from the neuronal network (passive network), the plateau did not occur. Additionally, the results of Fig. 7 (c) and (d) are remindful of the self-sustained discharges reported by Gorassini et al. (1998) in experiments with paired MUs in humans, suggesting that the latter results are also compatible with MN PICs.

When the synaptic input is frequency-modulated by a slowly varying triangle, the hysteresis observed in the torque (Fig. 6(a)) was due to differences in recruitment and de-recruitment of the MNs, as can be seen in Fig. 6(b) and Fig. 7. Biophysically, this difference is due to the activation of PICs, which cause a hysteresis in the f-I curve of individual AD MNs (Figs. 2 and 6(b)). Therefore, the value of the current required to recruit a given MN is larger than that required to turn off its discharge (Bennett et al. 1998; Lee and Heckman 1996, 1998b). It is important to emphasize that the motor behavior observed in the simulations is an emergent property of the network of model neurons acting under the influence of PICs.

Another experimental clue to the involvement of central mechanisms (e.g., PICs in the MNs) in the generation of force hysteresis is the existence of a similar hysteresis in the surface EMG, as suggested by the results of Fig. 8. This finding may suggest that recording also the EMG might be useful to distinguish between the contributions of central and peripheral mechanisms to the torque plateau and hysteresis. However, experimentally it will not be possible to assure that a central mechanism is exclusively due to PIC activation.

4.2 Effects of inhibition on torque generation

Experimental results on cats showed that the inhibition is functionally relevant in turning off the self-sustained discharge evoked by a brief excitatory input (Hounsgaard et al. 1988). In addition, several studies have reported that PIC magnitude and its effects on MN firing can be modulated by inhibitory synaptic inputs, for example, from the Ia reciprocal inhibition of antagonist muscles, resulting in a local control mechanism (Bennett et al. 1998; Hyngstrom et al. 2007; Hyngstrom et al. 2008; Johnson and Heckman 2010; Kuo et al. 2003). Here we have presented an example of the functional role of inhibition when a phasic force development is desired (Fig. 9(b)). The first assumption was that the spinal cord was under the influence of monoamines so that MN dendritic voltage-gated ionic channels (e.g., L-type Ca^{++} channels) are active. Under this condition, a brief excitatory synaptic input was sufficient to activate the PICs. This made the MNs keep discharging for a prolonged period and evoking a plateau in the torque (Figs. 5 and 9(a)). Without inhibition a high force TA contraction would have to be generated to counterbalance the maintained torque of the agonist muscle. The fast return of the torque caused by the descending inhibitory activity (Fig. 9(b)) emphasizes the importance of inhibitory inputs in networks whose MNs exhibit PICs, since in this situation, the PIC may be a limiting factor to the desired motor behavior and inhibition would be crucial to counterbalance its effects (Heckman et al. 2009; Johnson and Heckman 2010).

5 Conclusion

The first contribution of this work was the expansion of a public-domain large-scale neuromuscular simulator to include MN models that change their dynamic behavior in response to neuromodulatory activity. The simulator produced several results, for example, the torque plateau (or ET) and torque hysteresis for the TS muscle, hence supporting the hypothesis that motoneuronal PICs are responsible for these motor behaviors. Other functional contributions of dendritic PICs were also deduced from the model simulation results, such as the modulation of muscle force and the reduction in force variability, all depending upon the level of neuromodulation. Finally, the results suggested that inhibition has a fundamental importance in controlling phasic force generation when spinal cord neuromodulators are present. All these findings have implications on the understanding of human motor control and, to our knowledge this was the first theoretical-computational study that discussed such aspects. Some results are predictions that have to be tested by the experimental community, which is one of the roles of

computational neuroscience, *i.e.*, raising new questions for the experimental neuroscientists.

Acknowledgments This work was funded by FAPESP (State of São Paulo Funding Agency) and CNPq (The National Council for Scientific and Technological Development). L.A. Elias and V.M. Chaud hold scholarships from FAPESP (#2009/15802-0) and CNPq (#132776/2011-1), respectively. The authors are grateful to Dr. F.H. Magalhães for his insights and valuable discussions.

Conflict of interest statement The authors declare that there is no conflict of interest with any financial organization regarding the material discussed in this manuscript.

Appendix: Geometric and electrotonic properties of the motoneuron pool

The passive characteristics of each single MN model (see section 2.1.1) depended on the geometric and electrotonic properties of the cell (Equations A1 to A5), which were based on data from type-specified (*i.e.*, S-, FR-, and FF-type) cat MNs (Fleshman et al. 1988; Zengel et al. 1985). In this study, the parameters varied linearly within each type of MNs (see Table 3), resulting in a piece-wise linear approximation of how these parameters vary along the whole pool. Figure 10 shows an example for the range of rheobase currents adopted in the SOL MN pool. All the parameters were made equal for the different motor nuclei (*i.e.*, SOL, MG, LG, and TA) and the differences between them were only in the numbers of each MU type (Table 4).

$$g_c = \frac{2}{\frac{R_i \cdot l_D}{\pi \cdot r_D^2} + \frac{R_i \cdot l_S}{\pi \cdot r_S^2}} \tag{A1}$$

$$g_{lD} = \frac{2 \cdot \pi \cdot r_D \cdot l_D}{R_{m,D}} \tag{A2}$$

$$g_{lS} = \frac{2 \cdot \pi \cdot r_S \cdot l_S}{R_{m,S}} \tag{A3}$$

$$C_D = 2 \cdot \pi \cdot r_D \cdot l_D \cdot C_m \tag{A4}$$

$$C_S = 2 \cdot \pi \cdot r_S \cdot l_S \cdot C_m \tag{A5}$$

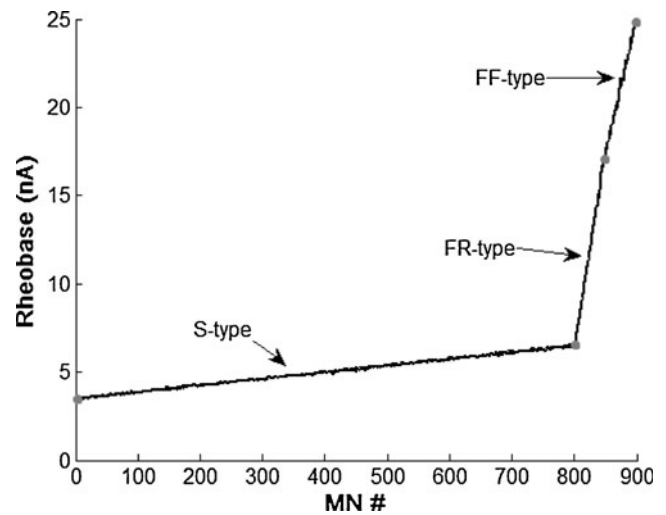


Fig. 10 Range of rheobase currents for the SOL MN pool. Within each MN type (the range is bounded by dots) the values varied linearly, resulting in a piece-wise linear variation along the pool

Table 3 Range of values adopted for the geometric and electrotonic parameters of MN models

Parameter	Unit	Value		
		S-type MU	FR-type MU	FF-type MU
Rheobase ^a	nA	3.50–6.50	6.50–17.50	17.50–25.10
Soma radius (<i>r_S</i>)	μm	38.75–41.25	41.25–43.75	43.75–56.50
Soma length (<i>l_S</i>)	μm	77.50–82.50	82.50–87.50	87.50–113
Soma specific resistance (<i>R_{m,S}</i>)	kΩ.cm ²	1.15–1.05	1.05–0.95	0.95–0.65
Dendrite radius (<i>r_D</i>)	μm	20.75–31.25	31.25–41.75	41.75–46.25
Dendrite length (<i>l_D</i>)	mm	5.50–6.80	6.80–8.10	8.10–10.60
Dendrite specific resistance (<i>R_{m,D}</i>)	kΩ.cm ²	14.40–10.70	10.70–6.95	6.95–6.05
Cytoplasm resistivity (<i>R_i</i>)	Ω.cm	70	70	70
Membrane specific capacitance (<i>C_m</i>)	μF/cm ²	1	1	1
Axon conduction velocity ^b	m/s	44–47	47–50	50–53

^a Rheobase values had a small variability (1 % of CV). ^b The distance between the MN pool and the muscles was equal to 0.66 m

Table 4 MU number adopted in each motor nucleus of the neuro-muscular system

Type	Plantarflexors			Dorsiflexor
	SOL	MG	LG	TA
S	800	250	200	250
FR	50	125	100	50
FF	50	125	100	50

References

- Bennett, D. J., Hultborn, H., Fedirchuk, B., & Gorassini, M. (1998). Synaptic activation of plateaus in hindlimb motoneurons of decerebrate cats. *Journal of Neurophysiology*, *80*(4), 2023–2037.
- Bergquist, A. J., Clair, J. M., & Collins, D. F. (2011). Motor unit recruitment when neuromuscular electrical stimulation is applied over a nerve trunk compared with a muscle belly: triceps surae. *Journal of Applied Physiology*, *110*(3), 627–637.
- Binder, M. D. (2002). Integration of synaptic and intrinsic dendritic currents in cat spinal motoneurons. *Brain Research Reviews*, *40*(1–3), 1–8.
- Binder, M. D., & Powers, R. K. (1999). Synaptic integration in spinal motoneurons. *Journal of Physiology, Paris*, *93*(1–2), 71–79.
- Cisi, R. R. L., & Kohn, A. F. (2008). Simulation system of spinal cord motor nuclei and associated nerves and muscles, in a Web-based architecture. *Journal of Computational Neuroscience*, *25*(3), 520–542. doi:10.1007/s10827-008-0092-8.
- Collins, D. F. (2007). Central contributions to contractions evoked by tetanic neuromuscular electrical stimulation. *Exercise and Sport Sciences Reviews*, *35*(3), 102–109. doi:10.1097/jes.0b013e3180a0321b.
- Collins, D. F., Bergquist, A. J. (2011). “Extra torque” during electrically evoked contractions in humans. *J Neurosci eLetters*. Available via <http://www.jneurosci.org/content/31/15/5579.long#responses>. Accessed 01 August 2011.
- Collins, D. F., Burke, D., & Gandevia, S. C. (2001). Large involuntary forces consistent with plateau-like behavior of human motoneurons. *Journal of Neuroscience*, *21*(11), 4059–4065.
- Collins, D. F., Burke, D., & Gandevia, S. C. (2002). Sustained contractions produced by plateau-like behaviour in human motoneurons. *J Physiol-London*, *538*(1), 289–301.
- Dean, J. C., Yates, L. M., & Collins, D. F. (2007). Turning on the central contribution to contractions evoked by neuromuscular electrical stimulation. *Journal of Applied Physiology*, *103*(1), 170–176. doi:10.1152/jappphysiol.01361.2006.
- Destexhe, A. (1997). Conductance-based integrate-and-fire models. *Neural Computation*, *9*(3), 503–514.
- Destexhe, A., Mainen, Z. F., & Sejnowski, T. J. (1994). An efficient method for computing synaptic conductances based on a kinetic-model of receptor-binding. *Neural Computation*, *6*(1), 14–18.
- ElBassiouny, S. M., Schuster, J. E., & Heckman, C. J. (2010). Persistent inward currents in spinal motoneurons: Important for normal function but potentially harmful after spinal cord injury and in amyotrophic lateral sclerosis. *Clinical Neurophysiology*, *121*(10), 1669–1679. doi:10.1016/j.clinph.2009.12.041.
- Elias, L. A., Kohn, A. F. (2010). Single neuron and network models in force control. In: 9th Neural Coding Workshop, Limassol, Cyprus, pp 31–32.
- Finkel, A. S., & Redman, S. J. (1983). The synaptic current evoked in cat spinal motoneurons by impulses in single group-Ia axons. *J Physiol-London*, *342*, 615–632.
- Fleshman, J. W., Segev, I., & Burke, R. E. (1988). Electrotonic architecture of type-identified alpha-motoneurons in the cat spinal-cord. *Journal of Neurophysiology*, *60*(1), 60–85.
- Frigon, A., Thompson, C. K., Johnson, M. D., Manuel, M., Hornby, T. G., & Heckman, C. J. (2011). Extra forces evoked during electrical stimulation of the muscle or its nerve are generated and modulated by a length-dependent intrinsic property of muscle in humans and cats. *Journal of Neuroscience*, *31*(15), 5579–5588. doi:10.1523/JNEUROSCI.6641-10.2011.
- Fuglevand, A. J., Winter, D. A., & Patla, A. E. (1993). Models of recruitment and rate coding organization in motor-unit pools. *Journal of Neurophysiology*, *70*(6), 2470–2488.
- Fuglevand, A. J., Dutoit, A. P., Johns, R. K., & Keen, D. A. (2006). Evaluation of plateau-potential-mediated ‘warm up’ in human motor units. *J Physiol-London*, *571*(Pt 3), 683–693.
- Gorassini, M. A., Bennett, D. J., & Yang, J. F. (1998). Self-sustained firing of human motor units. *Neuroscience Letters*, *247*(1), 13–16.
- Heckman, C. J. (1994). Computer-simulations of the effects of different synaptic input systems on the steady-state input-output structure of the motoneuron pool. *Journal of Neurophysiology*, *71*(5), 1727–1739.
- Heckman, C. J., & Lee, R. H. (1999). Synaptic integration in bistable motoneurons. *Peripheral and Spinal Mechanisms in the Neural Control of Movement*, *123*, 49–56.
- Heckman, C. J., Gorassini, M. A., & Bennett, D. J. (2005). Persistent inward currents in motoneuron dendrites: implications for motor output. *Muscle & Nerve*, *31*(2), 135–156. doi:10.1002/Mus.20261.
- Heckman, C. J., Mottram, C., Quinlan, K., Theiss, R., & Schuster, J. (2009). Motoneuron excitability: The importance of neuromodulatory inputs. *Clinical Neurophysiology*, *120*(12), 2040–2054. doi:10.1016/j.clinph.2009.08.009.
- Houngaard, J., Hultborn, H., Jespersen, B., & Kiehn, O. (1988). Bistability of alpha-motoneurons in the decerebrate cat and in the acute spinal cat after intravenous 5-hydroxytryptophan. *J Physiol-London*, *405*, 345–367.
- Hyngstrom, A. S., Johnson, M. D., Miller, J. F., & Heckman, C. J. (2007). Intrinsic electrical properties of spinal motoneurons vary with joint angle. *Nature Neuroscience*, *10*(3), 363–369. doi:10.1038/Nn1852.
- Hyngstrom, A. S., Johnson, M. D., & Heckman, C. J. (2008). Summation of excitatory and inhibitory synaptic inputs by motoneurons with highly active dendrites. *Journal of Neurophysiology*, *99*(4), 1643–1652. doi:10.1152/jn.01253.2007.
- Jacobs, B. L., & Fornal, C. A. (1997). Serotonin and motor activity. *Current Opinion in Neurobiology*, *7*(6), 820–825.
- Jacobs, B. L., Martin-Cora, F. J., & Fornal, C. A. (2002). Activity of medullary serotonergic neurons in freely moving animals. *Brain Research Reviews*, *40*(1–3), 45–52.
- Johnson, M. D., & Heckman, C. J. (2010). Interactions between focused synaptic inputs and diffuse neuromodulation in the spinal cord. *Ann Ny Acad Sci*, *1198*, 35–41. doi:10.1111/j.1749-6632.2010.05430.x.
- Kiehn, O., & Eken, T. (1998). Functional role of plateau potentials in vertebrate motor neurons. *Current Opinion in Neurobiology*, *8*(6), 746–752.
- Klakowicz, P. M., Baldwin, E. R. L., & Collins, D. F. (2006). Contribution of M-waves and H-reflexes to contractions evoked by tetanic nerve stimulation in humans. *Journal of Neurophysiology*, *96*(3), 1293–1302. doi:10.1152/jn.00765.2005.
- Kuo, J. J., Lee, R. H., Johnson, M. D., Heckman, H. M., & Heckman, C. J. (2003). Active dendritic integration of inhibitory synaptic inputs *in vivo*. *Journal of Neurophysiology*, *90*(6), 3617–3624. doi:10.1152/jn.00521.2003.
- Lee, R. H., & Heckman, C. J. (1996). Influence of voltage-sensitive dendritic conductances on bistable firing and effective synaptic current in cat spinal motoneurons *in vivo*. *Journal of Neurophysiology*, *76*(3), 2107–2110.
- Lee, R. H., & Heckman, C. J. (1998a). Bistability in spinal motoneurons *in vivo*: Systematic variations in persistent inward currents. *Journal of Neurophysiology*, *80*(2), 583–593.
- Lee, R. H., & Heckman, C. J. (1998b). Bistability in spinal motoneurons *in vivo*: systematic variations in rhythmic firing patterns. *Journal of Neurophysiology*, *80*(2), 572–582.
- Lee, R. H., & Heckman, C. J. (1999). Paradoxical effect of QX-314 on persistent inward currents and bistable behavior in spinal motoneurons *in vivo*. *Journal of Neurophysiology*, *82*(5), 2518–2527.
- Lee, R. H., & Heckman, C. J. (2000). Adjustable amplification of synaptic input in the dendrites of spinal motoneurons *in vivo*. *Journal of Neuroscience*, *20*(17), 6734–6740.
- Li, Y. R., Gorassini, M. A., & Bennett, D. J. (2004). Role of persistent sodium and calcium currents in motoneuron firing and spasticity in chronic spinal rats. *Journal of Neurophysiology*, *91*(2), 767–783. doi:10.1152/jn.00788.2003.

- Lloyd, D. P. (1949). Post-tetanic potentiation of response in monosynaptic reflex pathways of the spinal cord. *Journal of General Physiology*, 33(2), 147–170.
- Lytton, W. W. (1996). Optimizing synaptic conductance calculation for network simulations. *Neural Computation*, 8(3), 501–509.
- Magalhaes, F. H., & Kohn, A. F. (2010). Vibration-induced extra torque during electrically-evoked contractions of the human calf muscles. *Journal of Neuroengineering and Rehabilitation*, 7, 26. doi:10.1186/1743-0003-7-26.
- Menegaldo, L. L., de Toledo, F. A., & Weber, H. I. (2004). Moment arms and musculotendon lengths estimation for a three-dimensional lower-limb model. *Journal of Biomechanics*, 37(9), 1447–1453. doi:10.1016/j.jbiomech.2003.12.017.
- Nickolls, P., Collins, D. F., Gorman, R. B., Burke, D., & Gandevia, S. C. (2004). Forces consistent with plateau-like behaviour of spinal neurons evoked in patients with spinal cord injuries. *Brain*, 127, 660–670. doi:10.1093/Brain/Awh073.
- Schwindt, P. C., & Crill, W. E. (1980a). Properties of a persistent inward current in normal and TEA-injected moto-neurons. *Journal of Neurophysiology*, 43(6), 1700–1724.
- Schwindt, P. C., & Crill, W. E. (1980b). Role of a persistent inward current in moto-neuron bursting during spinal seizures. *Journal of Neurophysiology*, 43(5), 1296–1318.
- Stuart, G. J., & Redman, S. J. (1990). Voltage dependence of Ia reciprocal inhibitory currents in cat spinal motoneurons. *J Physiol-London*, 420, 111–125.
- Taylor, A. M., & Enoka, R. M. (2004). Quantification of the factors that influence discharge correlation in model motor neurons. *Journal of Neurophysiology*, 91(2), 796–814. doi:10.1152/jn.00802.2003.
- Williams, E. R., & Baker, S. N. (2009). Circuits generating corticomuscular coherence investigated using a biophysically based computational model. I. Descending systems. *J Neurophysiol*, 101(1), 31–41. doi:10.1152/jn.90362.2008.
- Zengel, J. E., Reid, S. A., Sybert, G. W., & Munson, J. B. (1985). Membrane electrical-properties and prediction of motor-unit type of medial gastrocnemius motoneurons in the cat. *Journal of Neurophysiology*, 53(5), 1323–1344.
- Zhou, P., & Rymer, W. Z. (2004). MUAP number estimates in surface EMG: template-matching methods and their performance boundaries. *Ann Biom Eng*, 32(7), 1007–1015.